Delft University of Technology

Instability of Rotating-Cone Boundary Layer in Axial Inflow
Effect of Cone Angle

Tambe, S.S.; Schrijer, F.F.J.; Gangoli Rao, A.; Veldhuis, L.L.M.

Important note
To cite this publication, please use the final published version (if applicable).
Please check the document version above.

Instability of Rotating-Cone Boundary Layer in Axial Inflow: Effect of Cone Angle

Sumit Tambe,* Ferry Schrijer,† Arvind Gangoli Rao,‡ and Leo Veldhuis§
Delft University of Technology, 2629 HS Delft, The Netherlands

Boundary-layer instability on a rotating cone induces coherent spiral vortices that are linked to the onset of laminar–turbulent transition. This type of transition is relevant to several aerospace systems with rotating components, e.g., aeroengine nose cones. Because a variety of options exist for the nose-cone shapes, it is important to know how their shape affects the boundary-layer transition phenomena. This study investigates the effect of varying cone angle on the boundary-layer instability on rotating cones facing axial inflow. It is found that increasing cone angle has a stabilizing effect on the boundary layer over rotating cones in axial inflow. The parameter space of Reynolds number Re_l and local rotational speed ratio S is experimentally explored to find the spiral vortex growth on rotating cones of half angle $\psi = 22.5°$, $45°$, and $50°$. The previously addressed cases of $\psi = 15°$ and $30°$ are also revisited. Increasing half-cone angle is found to have a stabilizing effect on the boundary layer on the rotating cones with $\psi \lesssim 45°$; i.e., the spiral vortex growth is delayed to higher Re_l and S. This effect diminishes when the half-cone angle increases from $\psi = 45°$ to $50°$. The spiral vortex angle ϵ decreases with increasing rotational speed ratio S for all the investigated cones, irrespective of the half-cone angle. However, the instability on the broader cones is found to induce shorter azimuthal wavelengths.

Nomenclature

C	=	constant
D	=	base diameter of a cone, m
I	=	digital pixel intensity (pixel count)
L	=	meridional length of a cone, m
n	=	azimuthal number of vortices
Re_L	=	inflow Reynolds number
Re_l	=	local Reynolds number
r	=	radius, m
S	=	rotational speed ratio
S_b	=	base rotational speed ratio
s	=	S^2, rotational speed ratio squared
U_∞	=	inflow velocity, m/s
u	=	meridional velocity, m/s
x, y	=	coordinate system aligned with the cone axis, m
x', y'	=	coordinate system aligned with the cone meridian, m
δ^*	=	boundary-layer thickness, $\sqrt{\nu/\omega}$, m
ϵ	=	spiral vortex angle, °
λ_θ	=	azimuthal wavelength, m
ν	=	kinematic viscosity, m²/s
ψ	=	half-cone angle, °
ω	=	angular velocity, rad/s

Subscripts

c	=	critical
m	=	maximum amplification
t	=	transition

Superscripts

m	=	exponent
$'$	=	fluctuation

I. Introduction

BOUNDARY-LAYER flows on rotating bodies are intriguing because their transition route involves instability-induced spiral vortex modes. Once formed, the spiral vortices undergo spatial growth in the downstream, where they start to alter the mean boundary-layer profile. The growing vortices enhance mixing as they bring the outer high-momentum fluid close to the rotating wall [1]. Beyond this region, the boundary layer starts to approach a turbulent state. This transition phenomenon is relevant to several aerospace systems, as they usually involve rotating components, and losses occur in their associated boundary layers. For example, the boundary layer entering an aeroengine core starts on the rotating cone. The state and flow topology of this boundary layer can influence the aerodynamic losses at the fan and compressor blade roots (evident from nonrotating cascade studies [2–4]), potentially affecting the overall engine efficiency. Therefore, it is of interest to investigate the boundary-layer instability behavior on rotating cones.

Generally, two types of instability mechanisms induce vortices on rotating cones: crossflow and centrifugal instability [5,6]. The crossflow instability appears when the meridional pressure gradient on the rotating cone creates inflectional velocity profile, similar to the ones observed on rotating disks [7] and swept wings [8]. This type of instability leads to vortices that are corotating in their cross sections [9,10]. On the other hand, the centrifugal instability is caused by the curved fluid motion. This type of instability is commonly observed in between rotating cylinders (Taylor vortices) [11], on concave walls (Görtler vortices) [12], etc. Recently, Kato et al. [13] showed that the Görtler number, which governs the instability on concave walls, also governs the centrifugal instability development on a rotating slender cone ($\psi = 30°$) in still fluid. The centrifugal instability usually induces vortices that are counter-rotating in their cross section.

When Kobayashi and Izumi [5] studied different rotating cones in still fluid, they found that the centrifugal instability occurs on rotating slender cones $\psi \lesssim 30°$ (which are closer to a rotating cylinder), whereas the crossflow instability appears on rotating broad cones $\psi \gtrsim 30°$ (which are closer to a rotating disk). The change in the instability mechanism occurs at approximately $\psi \approx 30°$, but the exact half-cone angle and conditions corresponding to this change are not

*Former Ph.D. Candidate, Aerospace Engineering; currently INSPIRE Faculty Fellow, Aerospace Engineering, Indian Institute of Science, Bangalore 560 012, India; sumittambe@iisc.ac.in.

†Scientific Director of Windtunnel Labs and Assistant Professor, Aerospace Engineering.

‡Professor and Chair of Sustainable Aircraft Propulsion Group, Aerospace Engineering.

§Professor and Head of AWEP Department, Aerospace Engineering.

known yet. Investigating this change of instability mechanism requires measurements/analyses of several cones with finely distributed half-cone angles, which is beyond the scope of this study.

To aeroengine nose cones, the case of a rotating cone in axial inflow (see Fig. 1) is more relevant than that in still fluid. A few past experiments have extensively investigated the rotating slender cone of $\psi = 15°$ in axial [14,15] and nonaxial inflows [16,17]. They show that the instability-induced spiral vortex growth on rotating cones depends on two flow parameters: local Reynolds number

$$Re_l = \frac{u_e l}{\nu} \qquad (1)$$

and local rotational speed ratio

$$S = \frac{r\omega}{u_e} \qquad (2)$$

Here, as depicted in Fig. 1, u_e is the boundary-layer edge velocity, l is the meridional length measured from the cone apex, ν is the kinematic viscosity, and ω is the angular velocity of the cone. Apart from their growth, the wavelength (or wavenumber) and wave angle of the spiral vortices are important instability characteristics. The azimuthal wavelength λ_θ is the circumferential spacing between the spiral vortices, relating to the azimuthal vortex number $n = 2\pi r/\lambda_\theta$. The spiral vortex angle ϵ is the angle of a spiral vortex with respect to the meridian. For a given cone, both n and ϵ depend only on the rotational speed ratio S [14,18].

Only limited cases of rotating cones ($\psi < 40°$) have been experimentally investigated in axial inflow [18,19]. However, in practice, the aeroengines' nose cones are found in a wide range of half-cone angles. Garrett et al. [20] theoretically investigated the effect of axial inflow on the boundary-layer instability on rotating broad cones ($\psi > 40°$). They predicted that the crossflow instability remains dominant on rotating broad cones with axial inflow, and that its onset depends on the same two flow parameters as in the case of slender cones: the local Reynolds number Re_l and rotational speed ratio S. Garrett et al. [20] explicitly highlighted the lack of experimental data to compare the theoretical predictions of crossflow instability on rotating broad cones in axial inflow. Therefore, it is necessary to extend the experimental investigations to larger half-cone angles $\psi \geq 15°$ to support the theoretical prediction methods.

This paper experimentally investigates the boundary-layer instability on both slender and broad cones rotating in axial inflow. The work extends from previously reported studies by the present authors Tambe et al. [16,19]. In Tambe et al. [16], it was shown how the nonaxial inflow delays the boundary-layer transition on a rotating slender cone of $\psi = 15°$, which was well-studied in the axial inflow by Kobayashi et al. [14]. In Tambe et al. [19], the spiral instability modes were detected on rotating cones ($\psi = 15°$, $30°$, and $40°$) for the first time under the inflow conditions pertaining to the real aeroengine in transonic flight, i.e., high-Reynolds-number inflow ($Re_l > 10^6$), low rotational speed ratio ($S < 1$–1.5), and Mach number $M = 0.5$. The present investigation focuses on exploring the parameter space of

Re_l and S to detect the spiral vortex growth for increasing cone angles, especially where theoretical data are available and experimental data are missing, i.e., $Rel < 10^5$, $S > 1$–1.5, incompressible flow, and for broad cones $\psi > 40°$. Additionally, the cases of rotating slender cones are also revisited for the sake of completeness. Cones with half-cone angles $\psi = 15°$, $22.5°$, $30°$, $45°$, and $50°$ are tested in axial inflow. The paper shows how the half-cone angle affects the spiral vortex growth, the instability-induced spiral vortex angle ϵ, and azimuthal vortex number n. The data are compared with the theoretical predictions of Garrett et al. [20] and the measurements of Kobayashi et al. [18].

Section II describes the experimental arrangement and data processing procedure. Section III shows visualizations of the spiral vortex footprints on the rotating cone surface for two broad cones ($\psi = 45°$ and $50°$) and a slender cone ($\psi = 22.5°$). Section IV shows how varying the half-cone angle affects the spiral vortex growth for all the investigated cones. Section V details the effect of half-cone angle on the spiral vortex angle ϵ and azimuthal vortex number n. Finally, Sec. VI summarizes conclusions of the present study.

II. Experiments

The experiments are performed in the W tunnel, a low-speed open-jet wind tunnel at Aerospace Engineering Faculty of Delft University of Technology (TU Delft). The size of the open-jet test section is 0.6×0.6 m^2. The freestream velocity U_∞ is varied from 0.7 to 10.9 m/s. The freestream turbulence level $u'_{\rm rms}$ is typically below 1% of U_∞.

The inflow Reynolds number Re_L and base rotational speed ratio S_b are used when referring to the operating conditions. These are defined as follows: $Re_L = U_\infty L/\nu$ and $S_b = D\omega/2U_\infty$. Here, U_∞ is the freestream velocity, L is the total meridional length of a cone, and D is the cone diameter.

Figure 2 shows the experimental arrangement. The cones are axially aligned with the freestream and rotated at 2900–13,500 r.p.m. using a brushless motor. First, the half-cone angles of $\psi = 15°$ and $30°$ are chosen for the investigations to compare with the previous measurements and theoretical results of Kobayashi et al. [18]. Additionally, a broad cone of $\psi = 50°$ is chosen to compare the experimental findings with the predictions of Garrett et al. [20]. Finally, a slender cone of $\psi = 22.5°$ and a broad cone of $\psi = 45°$ are also included in order to study intermediate values. All the cones have the same base diameter $D = 0.1$ m.

The instability-induced flow features (e.g., spiral vortices) are detected by measuring their thermal footprints on the rotating cone surface, following a previously reported method [15]. Here, surface temperature on rotating cones is measured using an infrared camera (see Fig. 2a). The cones are made of polyoxymethylene (POM) because it has favorable material properties for infrared thermography measurements. Viewing direction of the camera is adjusted to minimize the angle with respect to the surface normal, while avoiding the camera reflection from the cone surface (narcissus effect). The surface temperature is recorded as the digital pixel intensity I. The measurement contrast is increased by irradiating the cone by a 575 W theater lamp from the opposite side (see Fig. 2a). Table 1 details the specifications of the infrared thermography setup.

During the wind tunnel operation, the rotating cone slightly cools down due to the flow. This gradually reduces the temperature levels over the run. To remove this effect, a moving mean filter with a kernel size of 20 instances is subtracted from the raw dataset. This operation yields the temperature fluctuations I' with respect to a zero moving mean. This preprocessed data are referred to as raw data in the subsequent text. The dataset is further decomposed into POD (Proper Orthogonal Decomposition) modes to allow selective reconstruction of the spiral vortex footprints (see [15] for further details).

The meridional velocity field is measured using two-component high-speed particle image velocimetry (PIV) (see Fig. 2b). The data are acquired and processed using a commercial software DaVis 8.4.0. A multipass cross-correlation approach with decreasing interrogation window size (from 96×96 to 32×32 pixels) is used to obtain the instantaneous velocity vectors from the image pairs. Table 2 details the specification of the PIV setup.
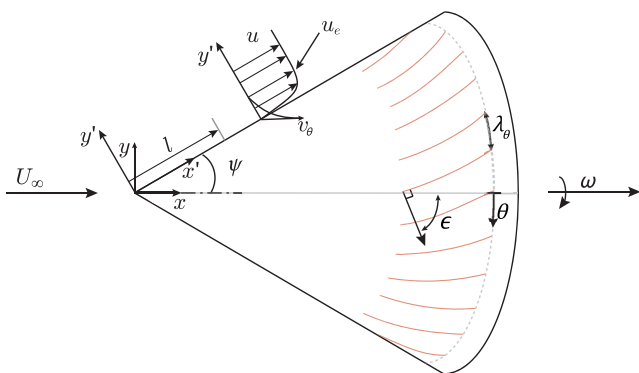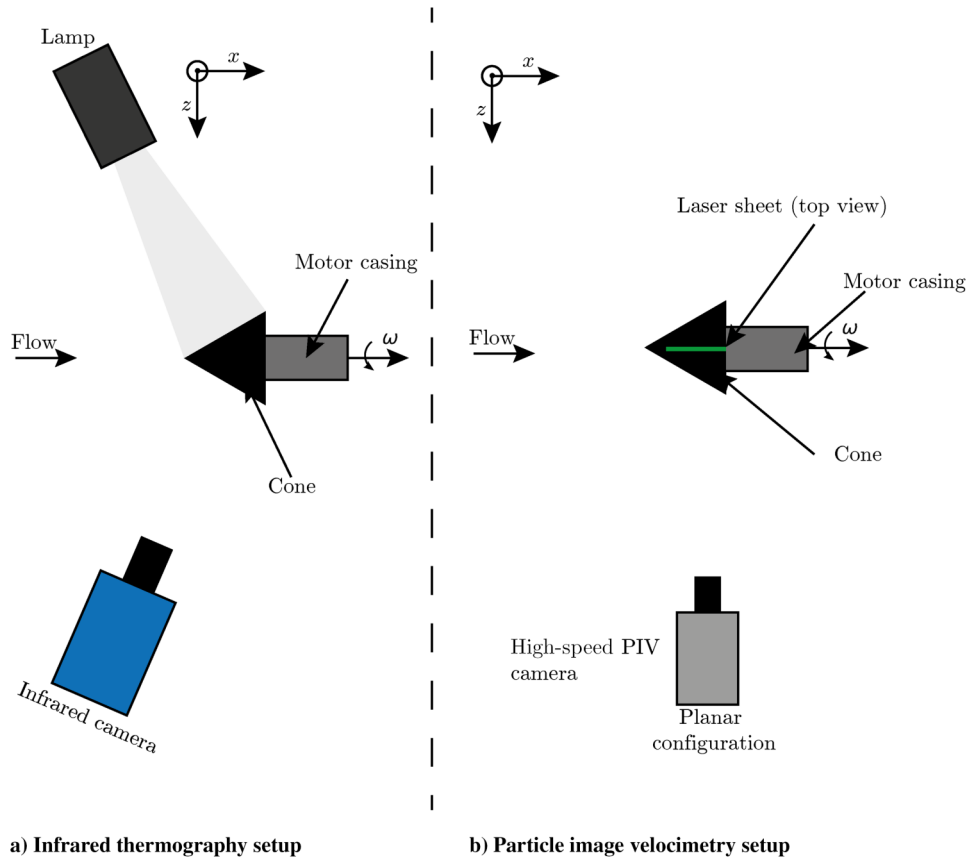

Fig. 1   Schematic of a rotating cone in axial inflow.

a) Infrared thermography setup   **b) Particle image velocimetry setup**

Fig. 2   Schematic of the experimental arrangements: a) infrared thermography and b) particle image velocimetry.

Table 1   Specifications of the infrared thermography setup

Camera	FLIR (CEDIP) SC7300 Titanium
Noise equivalent temperature difference (NETD)	25 mK
Spatial resolution	0.49–0.51 mm/px
Integration time	106–205 μs
Acquisition frequency	200 Hz
Number of images per dataset	2000
Heat source	Theater lamp (575 W)

Table 2   Specifications of the PIV setup

Camera	Photron Fastcam SA-1
Sensor dimensions	1024×1024 px
Vector pitch (2C)	0.26 mm
Interrogation window size	1.04 mm $\times$ 1.04 mm
Spatial resolution	30.7 px/mm
Laser	Nd:YAG Quantronix Darwin Duo 527-80-M
Acquisition frequency	2 kHz
Number of image pairs per dataset	2000
Seeding	Smoke particles (diameter ≈ 1 μm)

Generally, the instability characteristics of a flow-system depend on its basic flow [21]. As the instability-induced flow features grow upon this basic flow, they can significantly alter the basic velocity profiles. Previous studies [5,20,22] have shown that the boundary-layer edge velocity u_e of this basic flow can be assumed to be equal to the wall parallel velocity of the potential flow over a cone. This assumption leads to the form of $u_e = U_\infty Cl^m$, where m and C are determined for a given half-cone angle and freestream conditions. However, Kobayashi et al. [18] have shown that although the measured u_e closely follows the form $U_\infty Cl^m$ for the slender cones

($\psi = 7.5°$ and $15°$), it tends to be higher near the base of a broader cone ($\psi = 30°$). To facilitate comparisons with theory and past experiments, the boundary-layer edge velocity of the basic flow is assumed to be of the form $u_e = U_\infty Cl^m$, where C and m are determined by a least-square fit to the measurements away from the base and before the onset of the spiral vortices (e.g., see Fig. 3). Here, the boundary-layer edge velocity is measured from a time-averaged velocity field, at a location away from the wall where the vorticity value reduces to that of the measurement uncertainty ($<0.3U_\infty/D$). Figure 3 shows that measured boundary-layer velocity follows the form $u_e = U_\infty Cl^m$ at first but deviates toward the base of the cone, as expected. Table A1 in the Appendix details the parameters C and m for the investigated operating conditions.
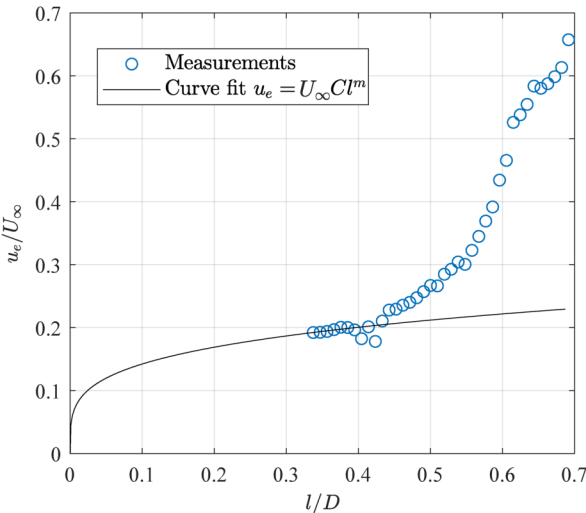

Fig. 3   An example showing the estimated edge velocity of the basic flow vs the measured edge velocity for $\psi = 45°$.

III. Visualization of Spiral Vortex Footprints

When spiral vortices grow in a boundary layer, they alter the surface-temperature pattern on a rotating cone. Due to their down-wash, the vortices increase the shear near the wall. This causes increased heat transfer between the fluid and the cone surface. Contrarily, upwash decreases such heat transfer. This causes cold/hot regions on the cone surface that are observed as darker/brighter regions in an infrared image, revealing the footprint of the spiral vortices.

Figure 4 visualizes different types of temperature fluctuation patterns on a rotating cone of $\psi = 50°$. Here, the top row contains the projections of a three-dimensional cone in a camera sensor plane, and the bottom row contains unwrapped images of the cone surface in polar coordinates l and θ. Figures 4a and 4d show a raw snapshot. Here, the spiral vortex footprints are subtle because the image is dominated by the noise from the infrared sensor. The spiral vortex footprints become distinctly clear in a low-order representation of the snapshot, as seen in Figs. 4c and 4f. This representation is reconstructed from the POD modes containing the azimuthal wavelength λ_θ between $\pi r/4$ and 4 px (see [15] for the details regarding the data reduction procedure).

However, the most striking pattern in the raw snapshot (Figs. 4a and 4d) is the dark and bright spiral with the azimuthal wavelength $\lambda_\theta \approx \pi r$. This pattern is isolated from the raw snapshot by reconstructing POD modes of azimuthal wavelengths $\lambda_\theta > \pi r/4$, as shown in Figs. 4b and 4e. The temperature fluctuations on the rotating cone involve two distinct patterns: a short-wavelength pattern ($\lambda_\theta < \pi r/4$) relating to the spiral vortices (Figs. 4c and 4f) and a long-wavelength pattern ($\lambda_\theta > \pi r/4$). Comparing Figs. 4b and 4c (or Figs. 4e and 4f) shows that the spiral vortices coexist with the long-wavelength pattern but their spacing starts to vary along the azimuth; i.e., their azimuthal coherence is disturbed in this region. The flow phenomenon in the region of long-wavelength pattern is further discussed in Sec. IV.

Figure 5 shows that the temperature fluctuation patterns on a rotating cone of $\psi = 45°$ is similar to that on a rotating $\psi = 50°$ cone (Fig. 4). Here, both short- and long-wavelength patterns exist. Together, Figs. 4 and 5 confirm the existence of the spiral vortices on rotating broad cones ($\psi > 30°$) in axial inflow.

Furthermore, the temperature fluctuation patterns on the rotating slender cone $\psi = 22.5°$ also show two types of spiral patterns on the broad cones; see Fig. 6 (the meridional lines at the bottom half of the images are background reflections from the surroundings, e.g., room heaters seen in Infrared camera and, therefore, unrelated to the flow). Previous studies [15], including the ones at high Reynolds number [19], have also shown the existence of two types of short- and long-wavelength patterns in the POD modes on a rotating cone of $\psi = 15°$. Recently, Kato et al. [23] studied a rotating broad cone ($\psi = 60°$) in still fluid and visualized the instability modes using patterns of the phase-averaged azimuthal velocity. Their visualization also shows short- and long-wavelength patterns. Overall, this indicates that the spiral vortices and the long-wavelength pattern are distinct features that appear in the transitional boundary layer on both slender and broad rotating cones.

IV. Spiral Vortex Growth

Since the spiral vortex growth on rotating slender cones ($\psi \lesssim 30°$) has been extensively investigated in the past [1,5,16], this section first focuses on the case of a rotating broad cone ($\psi \gtrsim 30°$) in axial inflow. The growth of the spiral vortices can be tracked through its effects on the surface temperature fluctuations and the velocity fields. To facilitate this, Fig. 7 compares the
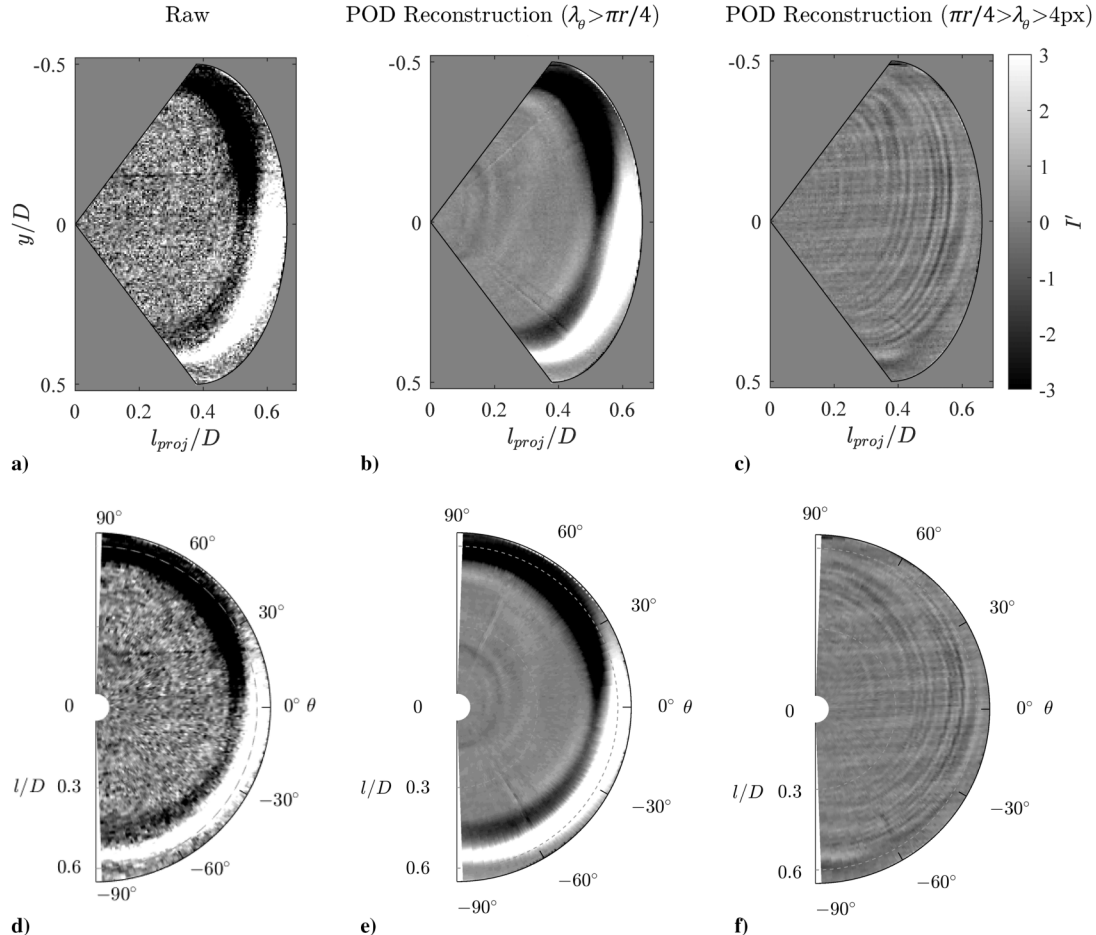
Fig. 4 Spiral vortex footprints on a rotating cone ($\psi = 50°$, $Re_L = 9.7 \times 10^3$, $S_b = 30.6$). Raw (a, d), and POD reconstruction of long wavelengths $\lambda_\theta > \pi r/4$ (b, e), and short wavelengths $\pi r/4 > \lambda_\theta > 4$ px (c, f); presented in the camera frame (top row) and as unwrapped views (bottom row).
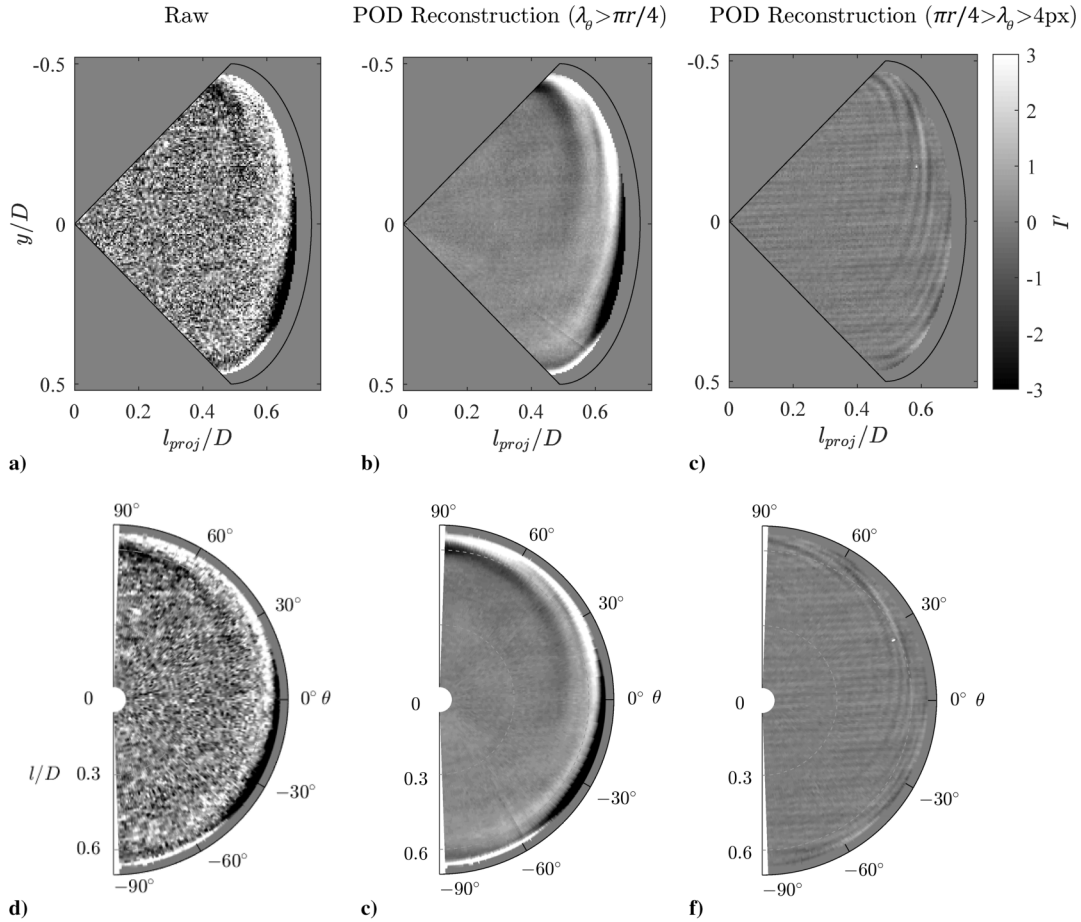
Fig. 5   Spiral vortex footprints on a rotating cone ($\psi = 45°$, $Re_L = 1 \times 10^4$, $S_b = 27.1$). Raw (a, d), and POD reconstruction of long wavelengths $\lambda_\theta > \pi r/4$ (b, e), and short wavelengths $\pi r/4 > \lambda_\theta > 4$ px (c, f); presented in the camera frame (top row) and as unwrapped views (bottom row).

following quantities on a rotating broad cone of $\psi = 50°$: root mean square (rms) of surface temperature fluctuations I'_{rms} along the meridian (Fig. 7a), time-averaged velocity field in a meridional plane (Fig. 7b), instantaneous vorticity field in a meridional plane (Fig. 7c), and a combined POD reconstruction of short- and long-wavelength patterns (Fig. 7d, relating to the snapshot in Fig. 4). Note that Figs. 7c and 7d represent uncorrelated instances.

As the spiral vortices start growing in the boundary layer, their surface temperature footprint starts to get stronger. This is evident from Fig. 7a, where I'_{rms} starts to increase at around $l/D \approx 0.4$. Around this location, the vorticity field in Fig. 7c shows a wavy pattern of predominantly positive vorticity, suggesting the presence of corotating spiral vortices. Such corotating spiral vortices have been previously linked to crossflow instability [24].

Further downstream in Fig. 7, at around $l/D \approx 0.5$, I'_{rms} suddenly increases. This meridional location is defined here as a critical location l_c where the spiral vortices start their rapid growth, and the corresponding critical Reynolds number is defined as $Re_{l,c} = l_c u_e/\nu$.

During their rapid growth, the spiral vortices reach maximum amplification at $l/D \approx 0.57$. Here, I'_{rms} reaches its peak (Fig. 7a). The meridional location of this peak is defined as the location of maximum amplification l_m. The corresponding Reynolds number is termed as the maximum amplification Reynolds number $Re_{l,m} = l_m u_e/\nu$. The time-averaged velocity field (Fig. 7b) reveals that, around the maximum amplification location, the spiral vortices start to significantly increase the near-wall momentum.

The enhanced mixing near the maximum amplification has also been observed for the centrifugal instability on the rotating slender cone of $\psi = 15°$ (see [1,16]). Furthermore, this marks a significant departure from the basic flow on the rotating cones, which is usually estimated without considering the effect of instability-induced spiral vortices (as seen in Fig. 3).

The instantaneous vorticity field (Fig. 7c) clearly shows how the vortices have amplified around the maximum amplification location $l/D \approx 0.57$. Here, as the spiral vortices amplify and move away from the wall, their counter-rotating part appears as a region of negative vorticity. This observation is similar to that of [14] for a $\psi = 30°$ cone rotating in still fluid. Those authors also observed that the spiral vortices first emerged as corotating and further downstream turned into a counter-rotating pair. Their observations show that the corotating spiral vortices rotate in the direction of positive vorticity as also observed in the present Fig. 7c. The present observations (for $\psi \leq 50°$) show that although on broad cones the spiral vortices may start as corotating, upon amplification they can turn into counter-rotating vortex pairs.

Figure 7d reveals that the long-wavelength pattern starts appearing close to the critical point $l/D \approx 0.5$. As it is overlaid on the short-wavelength spiral vortex footprints, the long-wavelength pattern represents the azimuthal modulation of the rapidly growing spiral vortices. Usually, several complex interactions occur during the spiral vortex growth, e.g., variations in the azimuthal spacing of the spiral vortices and occasional instances of vortex pairing (Fig. 4 and [16]), and appearance of the counter-rotating part of the growing corotating vortices (Fig. 7 and [14]). Therefore, ascertaining the origin of the long-wavelength mode and its role in the spiral vortex amplification requires further investigations, including nonlinear and nonparallel effects.

Both the centrifugal and crossflow instabilities on rotating cones depend on the local rotational speed ratio S and local Reynolds number Re_l [5,20]. For a given rotating cone, the maximum amplification Reynolds number $Re_{l,m}$ follows an exponential relation with the local rotational speed ratio S (see Fig. 8). For all cones, with increasing local rotational speed ratio S, the maximum amplification occurs at a lower local Reynolds number Re_l. This is because the increased rotation strength S increasingly destabilizes the boundary layer.
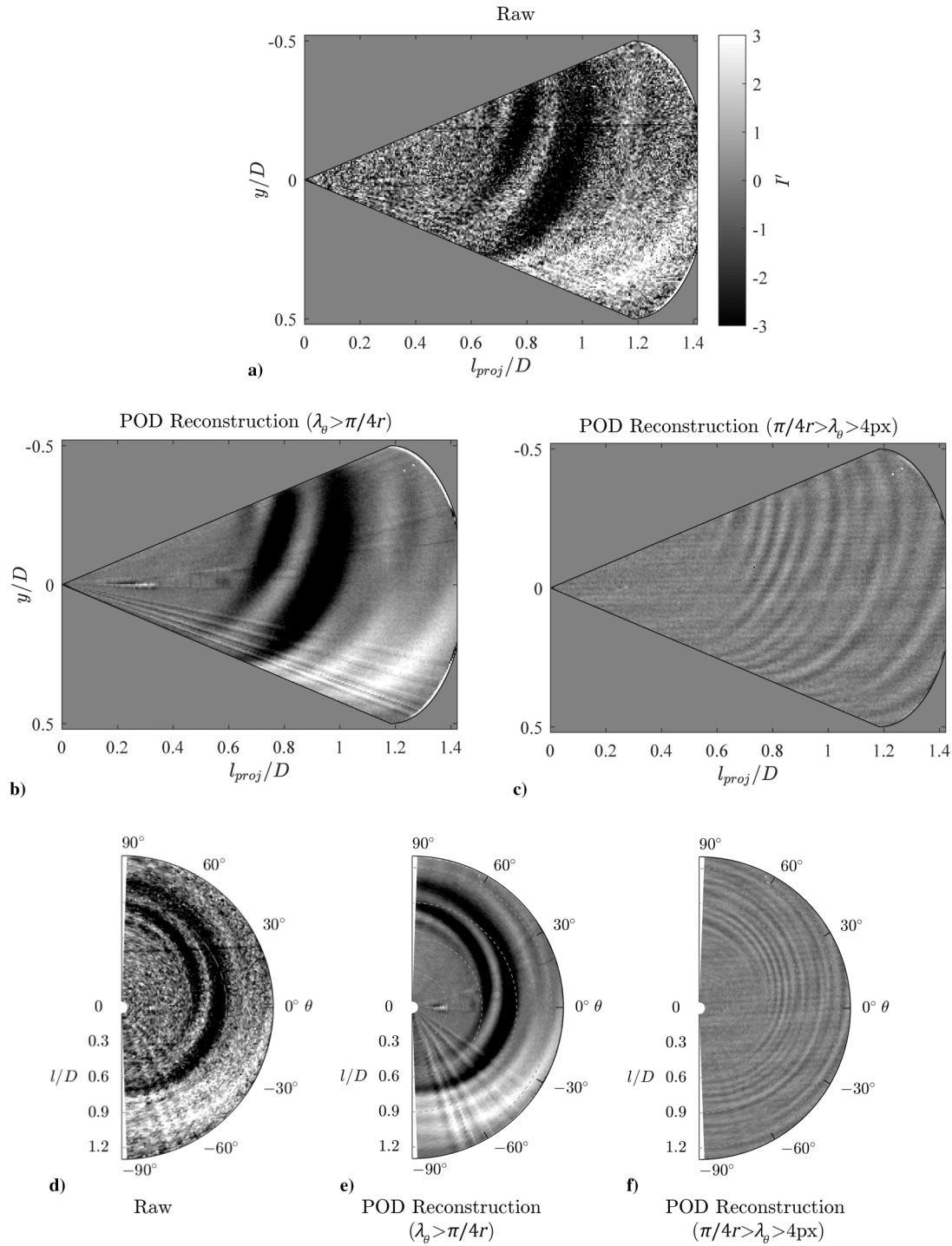
Fig. 6   Spiral vortex footprints on a rotating cone ($\psi = 22.5°$, $Re_L = 8.1 \times 10^4$, $S_b = 2.9$). Raw (a, d), and POD reconstruction of long wavelengths $\lambda_\theta > \pi r/4$ (b, e), and short wavelengths $\pi r/4 > \lambda_\theta > 4$ px (c, f); presented in the camera frame (top row) and as unwrapped views (bottom row). (The meridional lines at the bottom half of the images are background reflections from the surroundings, e.g., room heaters seen in Infrared camera, and therefore unrelated to the flow.)

Figure 8 suggests that, at first, increasing the half-cone angle stabilizes the boundary layer on rotating cones; i.e., the maximum amplification occurs at higher Re_l and S for broader cones. However, for large half-cone angles $\psi = 45°$ and $50°$ the maximum amplification is not significantly affected by varying the half-cone angle. Kobayashi et al. [14] observed a similar behavior on rotating cones in still fluid. They observed that the critical Reynolds number is highly sensitive to the changes in low half-cone angles ($\psi \lesssim 40$–$45°$), but becomes less sensitive to the changes in high half-cone angles ($\psi \gtrsim 40$–$45°$) (see [5]).

Furthermore, Fig. 8 also compares the results of two different tests on the slender cones ($\psi = 15°$) of two base diameters: $D = 0.1$ m in

the present work and $D = 0.047$ m from [16]. All these tests were conducted in the same wind tunnel facility (W tunnel). The maximum amplification locations from both the tests show the same trend in $Re_l - S$ parameter space. This confirms a good repeatability of the present experimental approach in determining the maximum amplification of the spiral vortices.

The present operating conditions are at low inflow Reynolds number $Re_L < 10^5$ and consequently at high base rotational speed ratio $S_b > 1$. However, during a typical transonic cruise, aeroengines operate at high inflow Reynolds number $Re_L > 10^6$ and low base rotational speed ratio $S_b < 1$ [19]. Figure 9 compares the present measurements to those at inflow conditions pertaining to
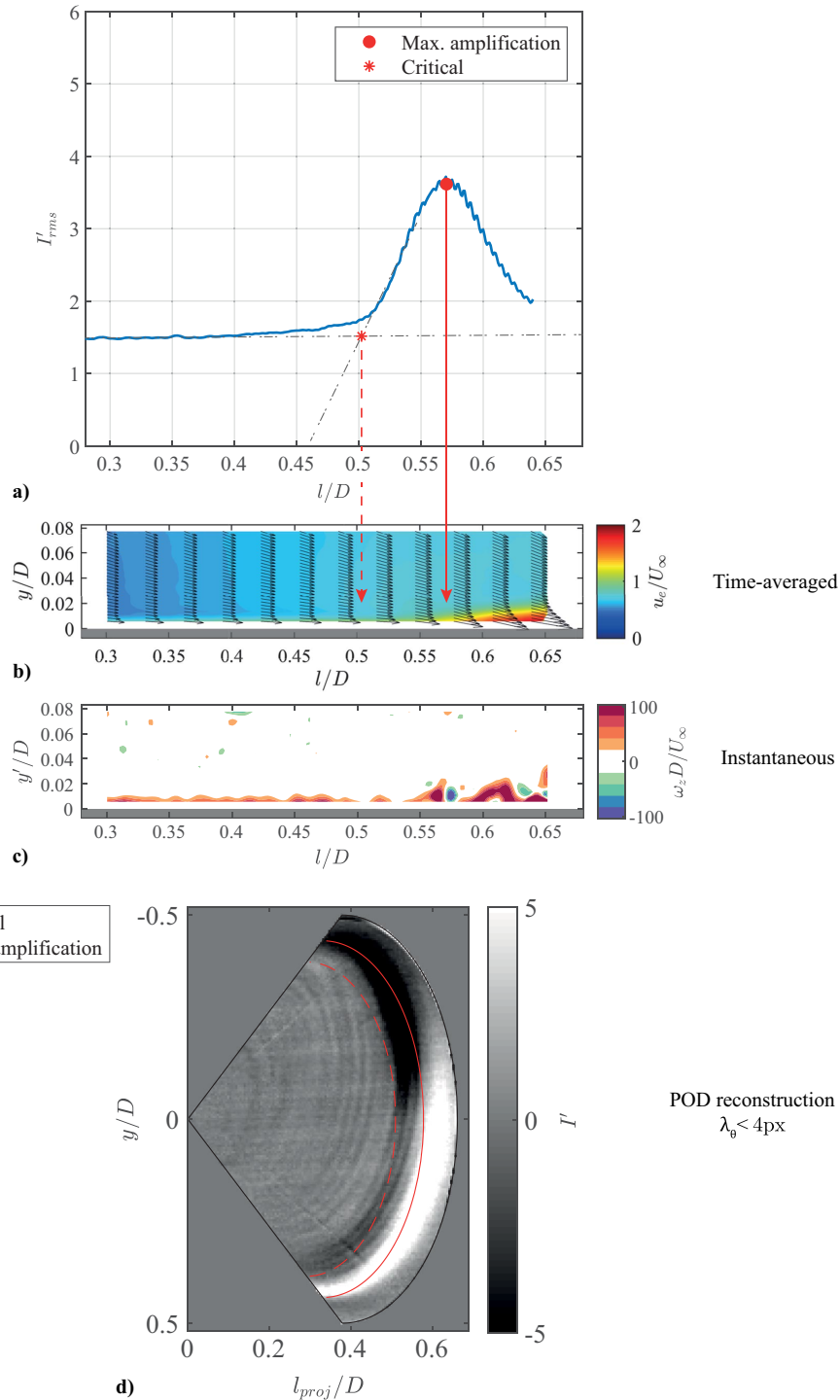
Fig. 7 Growth of the spiral vortices on a rotating cone ($\psi = 50°$, $Re_L = 9.7 \times 10^3$, $S_b = 30.6$). a) A meridional trace of surface temperature fluctuations I'_{rms}, b) time-averaged velocity field, c) instantaneous vorticity field in a meridional plane, and d) a combined POD reconstruction of short- and long-wavelength temperature patterns (criterion $\lambda_\theta > 4$ px).

typical aeroengines. Here, maximum amplification $Re_{l,m}$ shows a well-behaved relation with the local rotational speed ratio S as $Re_{l,m} = C_1 S^a$. The present measurements show that for $\psi = 30°$, $a = -1.62$ and $C_1 = 7.2 \times 10^5$. For $\psi = 15°$, $a = -2.62$ and $C_1 = 2.3 \times 10^5$ [19]. The high-Reynolds-number measurements are not available for the broad cones of $\psi = 45°$ and $50°$, but their corresponding $Re_{l,m} - S$ trend is expected to continue till a high Reynolds number.

For all cone types, the critical Reynolds number $Re_{l,c}$ decreases with the rotational speed ratio S (see Fig. 10). Past studies have shown that, unlike the Reynolds numbers at maximum amplification and turbulence onset, the critical Reynolds number is sensitive to the

disturbance environment, i.e., freestream turbulence level [14,18,19], unavoidable dust motes, and surface imperfections [25]. Nevertheless, similar to the maximum amplification, the critical Reynolds number shows a high sensitivity to the changes in low half-cone angles ($\psi \lesssim 45°$). The critical Reynolds number is not significantly affected by the changes in high half-cone angles ($\psi = 45$–$50°$). This agrees with the observations made by [14] on rotating cones in still fluid.

Garrett et al. [20] have theoretically predicted the onset of convective crossflow instability in a range of broad cones rotating in axial inflow by identifying the critical instability points in the space of Reynolds number $Re_{\delta^*} = \delta^* l \sin(\psi)\omega/\nu$ and a parameter
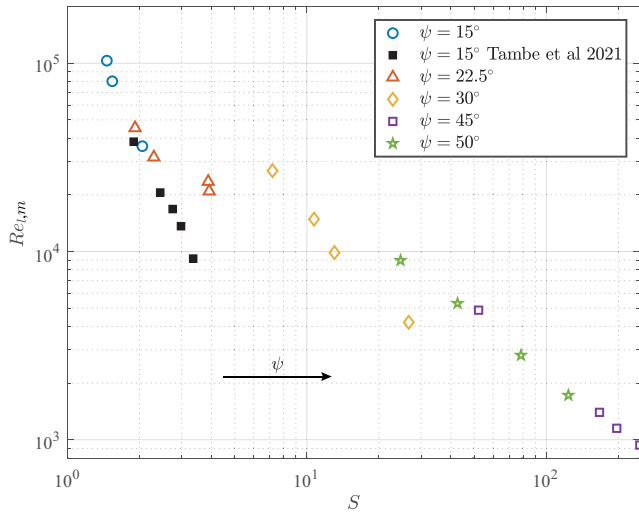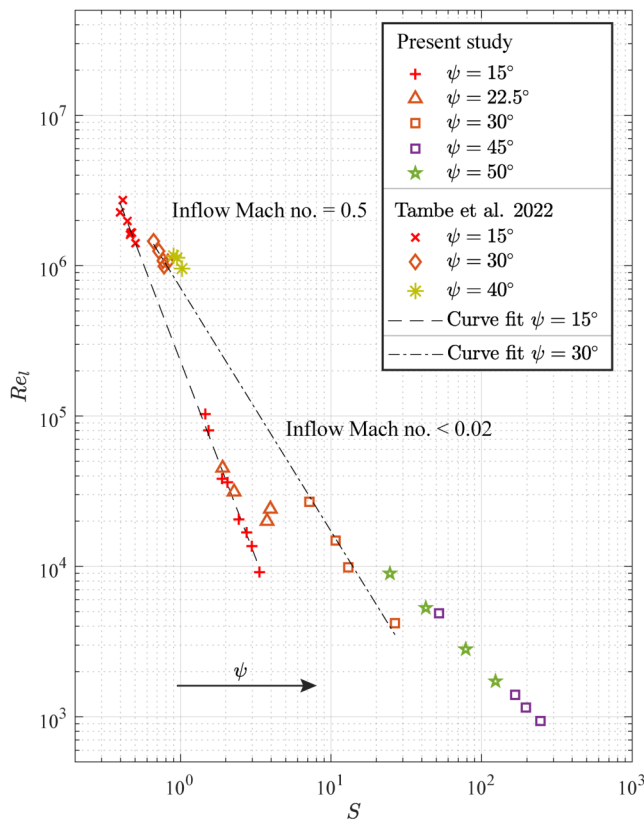
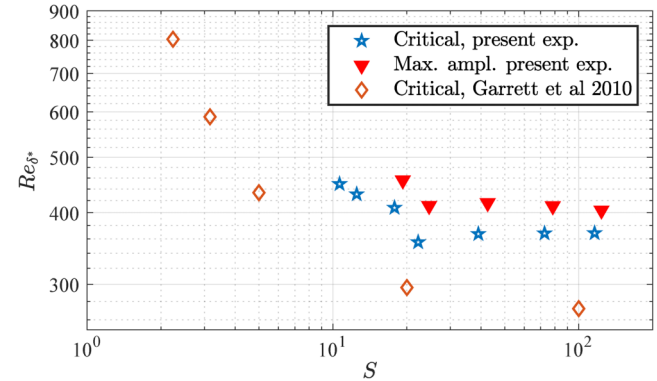**Fig. 8   Effect of half-cone angle on the maximum amplification of spiral vortices.**
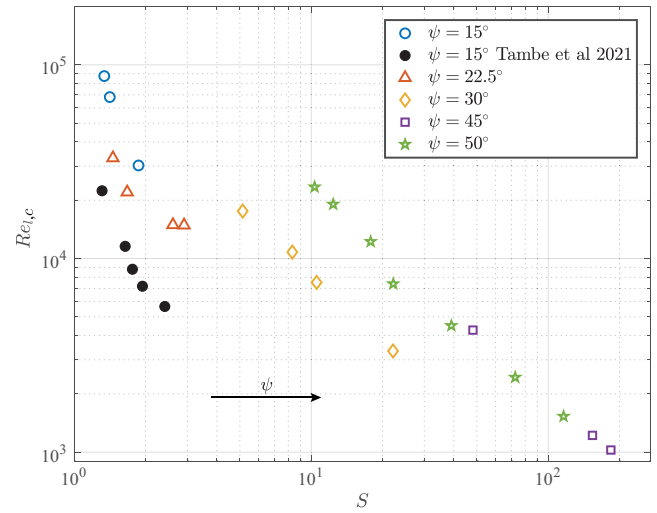
Fig. 10   Effect of half-cone angle on the critical point relating to the rapid growth of the spiral vortices.
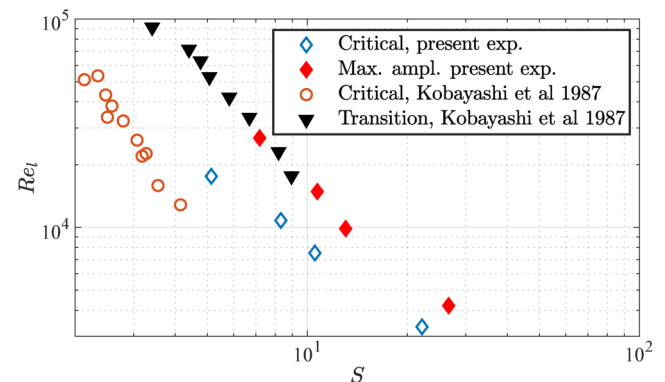

Fig. 9   Maximum amplification Reynolds number ($Re_{l,m}$) from the present study compared to the high-speed investigations from the literature [19], relating to the aeroengine operating regime.

Fig. 11   Comparison of the present experiments with the theoretical predictions of [20] for a rotating broad cone of $\psi = 50°$ in axial inflow.

Kobayashi et al. [18] have measured the spiral vortex growth on a rotating broad cone of $\psi = 30°$ in axial inflow. They defined a critical point as the point where the hot-wire signal starts to show velocity fluctuations of single frequency, measured 0.5 mm away from the cone surface. Furthermore, they defined the transition point as the most-upstream location where a wide spectrum of the velocity fluctuations (representative of turbulence) was measured. Figure 12 compares the present measurements to those of [18] for a rotating cone of $\psi = 30°$ in axial inflow. Trends in both the studies agree, and overall, the regions of spiral vortex growth overlap in $Re_l - S$ parameter space. Furthermore, the maximum amplification

$s = (l \sin(\psi) \omega / u_e)^2 = S^2$. Here, the length scale $\delta^* = \sqrt{\nu/\omega}$ relates to the boundary-layer thickness on a rotating cone, without accounting for the effect of axial inflow. Figure 11 compares the present measurements of critical and maximum amplification points on a broad cone of $\psi = 50°$ to the critical points predicted by [20]. The trends of experimental and theoretical data agree with each other. However, the measured critical Reynolds number is higher than the theoretical prediction. Garrett et al. [20] had highlighted that their parallel flow assumption could lead to the quantitative differences. Therefore, further theoretical analysis with revised base flow computation and combined experimental data are necessary to address the quantitative differences.

Fig. 12   Comparison of the present experiments with the measurements of [18] on a rotating cone of $\psi = 30°$ in axial inflow.

points in the present study coincide with the transition points measured by [18]. The critical points in the present measurements appear at higher Reynolds number and rotational speed ratio as compared to the measurements of [18]. This is ascribed to differences in the definitions, measurement techniques, and measurement sensitivities.

V. Spatial Characteristics of the Spiral Vortices

From the instability standpoint, two characteristics of the spiral vortices are important: spiral vortex angle ϵ and azimuthal number of vortices n. These characteristics are useful inputs in theoretical stability analyses that assess the system stability for perturbation waves of different orientation ϵ and wave number n. In the present study, ϵ and n are obtained by projecting the instantaneous low-order reconstructions of the spiral vortices (e.g., Fig. 4c) onto the xy plane. The angle ϵ is obtained as an angle between a linear fit through the extrema of I' along a spiral vortex footprint (within $y/D \approx -0.07 - 0.07$) and $y/D = 0$. The azimuthal number n is obtained by counting the peaks of I' along the y coordinate for several axial locations (see [16] for further details). The measurement uncertainty is of the order of $\pm 1°$ for the spiral vortex angle ϵ and ± 1 for the azimuthal vortex number n.

All investigated cases show a wide range of spiral vortex angles ϵ at a given rotational speed ratio S (see Fig. 13). This relates to the fact that while growing, the azimuthal coherence of the spiral vortices starts to get disturbed, i.e., their azimuthal spacing and orientation varies. Typically, the theory predicts the

spiral vortex angles of the most unstable mode for a given rotational speed ratio S at the critical point [5,20,26]. However, the measurements detect the spiral vortex footprints once they have grown stronger where interaction phenomena, e.g., vortex pairing, lead to a wide range of spiral vortex angle, similar to the measurements of [5,18].

For all the investigated cones, the spiral vortex angle ϵ decreases with increasing rotational speed ratio S (see Fig. 13). This can be explained by the fact that the spiral vortices tend to align toward the local direction of the skewed boundary-layer velocity (in the cone reference frame). The trend agrees with the predictions of [20] for $\psi = 50°$ and measurements of [18]. It should be noted that Kobayashi et al. [18] measured the angle using a hot wire located at a fixed distance away from the rotating cone surface. However, the present measurements are performed at the cone surface. Therefore, the quantitative differences are ascribed to the different measurement locations.

The measured azimuthal vortex number n agrees with the data of [18] for a half-cone angle $\psi = 15°$ (see Fig. 14). Generally, the azimuthal vortex number n decreases with increasing rotational speed ratio S, for a given half-cone angle. This suggests that, when the rotation is stronger compared to the axial inflow, larger azimuthal wavelengths $\lambda_\theta = 2\pi r/n$ grow in the boundary layer.

Figure 14 shows that broad cones $\psi = 45°$ and $50°$ exhibit lower azimuthal number n compared to the predictions of [20] but show a similar trend of decreasing n with increasing S. As experiments also involve nonlinear effects, the observed azimuthal number n is usually expected to differ from the linear theory predictions [27]. The present
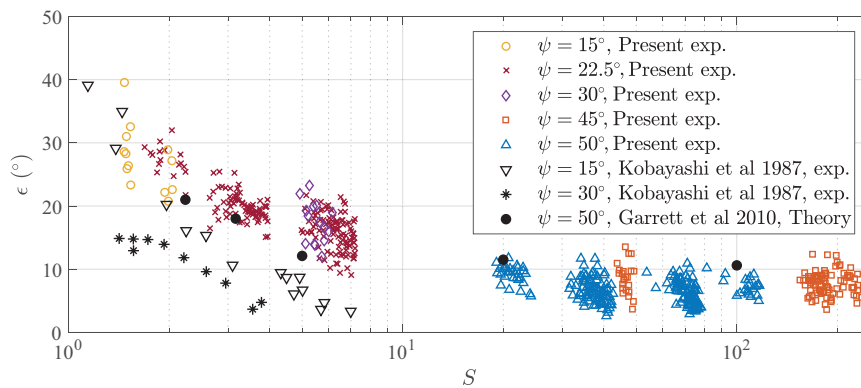

Fig. 13 Variation of the spiral vortex angle ϵ vs rotational speed ratio S for all the investigated cones, compared with the past measurements [18] and theory [20].
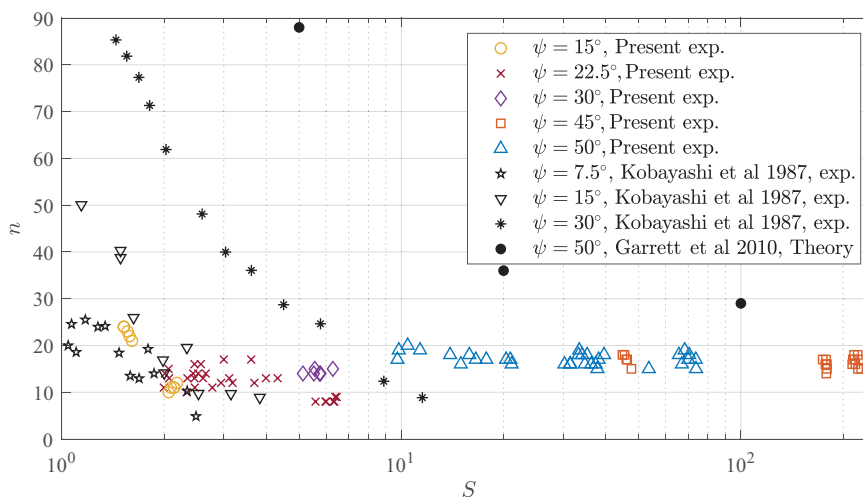

Fig. 14 Variation of the azimuthal vortex number n with rotational speed ratio S for all the investigated cones, compared with the past measurements [18] and theory [20].

measurements agree with those of [18] for $\psi = 15°$. Figure 14, including the past measurements and predictions, shows that with increasing half-cone angle the azimuthal vortex number n increases. However, broad cones of $\psi = 45°$ and $50°$ seem to have a common trend of n with respect to the rotational speed ratio S.

VI.   Conclusions

This study investigated the effect of the half-cone angle on the boundary-layer instability of rotating cones in axial inflow. The rotating slender cones of half-cone angle $\psi = 15°$ and $22.5°$, and rotating broad cones of half-cone angles $\psi = 30°$, $45°$, and $50°$ were tested in axial inflow. The parameter space of local Reynolds number Re_l and rotational speed ratio S was explored to detect the spiral vortices on rotating broad cones of $\psi = 45°$ and $50°$ for the first time. The surface temperature patterns on the rotating cones were measured using infrared camera and processed with the POD-based data reduction approach. Additionally, PIV measurements were used to obtain the meridional velocity field. Following are the important conclusions from this study:

• In all the investigated axial inflow conditions, the boundary-layer instability is found to induce spiral vortices on rotating cones of $\psi = 15°$–$50°$.

• The boundary-layer transition on all the investigated rotating cones show two distinct types of surface temperature fluctuation patterns: a short-wavelength pattern of $\lambda_\theta < \pi r/4$ relating to the spiral vortex footprints and a long-wavelength pattern of $\lambda_\theta > \pi r/4$ overlaid on the spiral vortex footprints. The latter occurs where the spiral vortices start their rapid growth. Further investigation is required to assess its role in the spiral vortex amplification.

• For all the investigated cones, the spiral vortices are found to affect the near-wall momentum in proximity of the point of their maximum amplification.

• On rotating broad cones, the spiral vortices appear to start as corotating but turn into counter-rotating type upon their amplification.

• For the rotating cones of $\psi < 45°$, increasing half-cone angle ψ has a stabilizing effect on the boundary layer. This delays the spiral vortex growth to higher local Reynolds number Re_l and higher rotational speed ratio S.

• For the rotating broad cones of $\psi = 45°$ and $50°$, the change in half-cone angle does not seem to have any significant effect on the location of spiral vortex growth in $Re_l − S$ parameter space. In both cases, the critical and maximum amplification points coincide on a seemingly common trend in $Re_l − S$ parameter space. A similar observation was reported by [18] for rotating cones in still fluid where the critical and transition Reynolds numbers are less affected by such broad half-cone angles $\psi \gtrsim 40$–$45°$.

• For $\psi = 50°$, the trends of measured critical and maximum amplification points agree with the trend of critical points predicted by [20], supporting their theory. The quantitative differences suggest the need of further investigation with combined experiments and theory.

• The present measurements of maximum amplification Reynolds number $Re_{l,m}$ follow a trend that extends well to those in high-Reynolds-number inflow [19] pertaining to the inflow conditions to aeroengines at transonic flight.

• The spiral vortex angle ϵ varies with the rotational speed ratio S. The variation is found to follow a common trend for all the investigated cases of rotating cones. The trend shows a qualitative agreement with the past measurements [18] and predictions [20].

• The azimuthal vortex number n decreases with increasing rotational speed ratio S for each cone. Together with the past measurements and predictions, the increasing half-cone angle results in higher azimuthal vortex number. This suggests that as the cones get broader, their instability induces spiral vortices with shorter azimuthal wavelengths.

Appendix: Basic Flow Parameters

Table A1   Parameters related to the boundary-layer edge velocity of the estimated basic flow $u_e = U_\infty Cl^m$ for different operating conditions

ψ	Re_L	S_b	C	m
15°	1.3×10^5	1.89	1.81	0.31
15°	9.7×10^4	1.94	1.81	0.31
15°	6.2×10^4	3.1	1.81	0.31
22.5°	2.8×10^4	5.24	1.18	0.07
22.5°	4.2×10^4	5.59	1.07	0.07
22.5°	6.6×10^4	3.56	1.04	0.07
22.5°	8.1×10^4	2.89	1.1	0.07
30°	8.0×10^3	28.45	1.05	0.117
30°	1.46×10^4	15.7	1.22	0.117
30°	2.13×10^4	10.8	1.12	0.117
30°	3.2×10^4	7.1	1.2	0.117
45°	3.35×10^3	97.6	0.9	0.248
45°	3.35×10^3	83.4	0.55	0.248
45°	5.68×10^3	49.24	0.38	0.248
45°	1.03×10^4	27	0.87	0.248
50°	4.09×10^4	7.23	1.47	0.3
50°	3.33×10^4	9	1.54	0.3
50°	2.39×10^4	12.44	1.42	0.3
50°	1.64×10^4	18	1.5	0.3
50°	3.14×10^3	94.36	1.55	0.3
50°	5.32×10^3	55.66	1.46	0.3

Acknowledgments

References

[1] Kohama, Y., "Behaviour of Spiral Vortices on a Rotating Cone in Axial Flow," *Acta Mechanica*, Vol. 51, Nos. 3–4, 1984, pp. 105–117.
https://doi.org/10.1007/BF01177066

[2] Lei, V.-M., Spakovszky, Z. S., and Greitzer, E. M., "A Criterion for Axial Compressor Hub-Corner Stall," *Journal of Turbomachinery*, Vol. 130, No. 3, 2008, Paper 031006, http://turbomachinery.asmedigital collection.asme.org/article.aspx?articleid=1467743.
https://doi.org/10.1115/1.2775492

[3] Scillitoe, A. D., Tucker, P. G., and Adami, P., "Numerical Investigation of Three-Dimensional Separation in an Axial Flow Compressor: The Influence of Freestream Turbulence Intensity and Endwall Boundary Layer State," *Journal of Turbomachinery*, Vol. 139, No. 2, 2017, pp. 1–10.
https://doi.org/10.1115/1.4034797

[4] Hergt, A., Meyer, R., and Engel, K., "Effects of Vortex Generator Application on the Performance of a Compressor Cascade," *Journal of Turbomachinery*, Vol. 135, No. 2, 2013, pp. 1–10.
https://doi.org/10.1115/1.4006605

[5] Kobayashi, R., and Izumi, H., "Boundary-Layer Transition on a Rotating Cone in Still Fluid," *Journal of Fluid Mechanics*, Vol. 127, Feb. 1983, pp. 353–364.
https://doi.org/10.1017/S0022112083002761

[6] Kobayashi, R., "Review: Laminar-to-Turbulent Transition of Three-Dimensional Boundary Layers on Rotating Bodies," *Journal of Fluids Engineering*, Vol. 116, No. 2, 1994, pp. 200–211.
https://doi.org/10.1016/j.ymssp.2015.09.042

[7] Lingwood, R. J., "Absolute Instability of the Boundary Layer on a Rotating Disk," *Journal of Fluid Mechanics*, Vol. 299, Sept. 1995, pp. 17–33.
https://doi.org/10.1016/j.euromechflu.2006.08.002

[8] Kohama, Y. P., "Three-Dimensional Boundary Layer Transition Study," *Current Science*, Vol. 79, No. 6, 2000, pp. 800–807.

[9] Kato, K., Alfredsson, P. H., and Lingwood, R. J., "Boundary-Layer Transition over a Rotating Broad Cone," *Physical Review Fluids*, Vol. 4,

No. 7, 2019, Paper 71902.
https://doi.org/10.1103/PhysRevFluids.4.071902

[10] Kato, K., Kawata, T., Alfredsson, P. H., and Lingwood, R. J., "Investigation of the Structures in the Unstable Rotating-Cone Boundary Layer," *Physical Review Fluids*, Vol. 4, No. 5, 2019, pp. 1–30.
https://doi.org/10.1103/PhysRevFluids.4.053903

[11] Taylor, G. I., "Stability of Viscous Liquid Contained Between Two Rotating Cylinders," *Philosophical Transactions of the Royal Society of London: Series A, Containing Papers of a Mathematical or Physical Character*, Vol. 223, Nos. 605–615, 1923, pp. 289–343.
https://doi.org/10.1002/zamm.19590391204

[12] Gortler, H., "On the Three-Dimensional Instability of Laminar Boundary Layers on Concave Walls," NACA Technical Memorandum 1375, 1954, https://ntrs.nasa.gov/citations/19930093855.

[13] Kato, K., Segalini, A., Alfredsson, P. H., and Lingwood, R. J., "Instability and Transition in the Boundary Layer Driven by a Rotating Slender Cone," *Journal of Fluid Mechanics*, Vol. 915, May 2021, pp. 1–11.
https://doi.org/10.1017/jfm.2021.216

[14] Kobayashi, R., Kohama, Y., and Kurosawa, M., "Boundary-Layer Transition on a Rotating Cone in Axial Flow," *Journal of Fluid Mechanics*, Vol. 127, Feb. 1983, pp. 353–364.
https://doi.org/10.1017/S0022112083002761

[15] Tambe, S., Schrijer, F., Rao, A. G., and Veldhuis, L., "An Experimental Method to Investigate Coherent Spiral Vortices in the Boundary Layer over Rotating Bodies of Revolution," *Experiments in Fluids*, Vol. 60, No. 7, 2019, p. 115.
https://doi.org/10.1007/s00348-019-2756-8

[16] Tambe, S. S., Schrijer, F., Rao, A. G., and Veldhuis, L., "Boundary Layer Instability over a Rotating Slender Cone Under Non-Axial Inflow," *Journal of Fluid Mechanics*, Vol. 910, March 2021, p. A25.
https://doi.org/10.1017/jfm.2020.990

[17] Tambe, S., Schrijer, F., Rao, A. G., and Veldhuis, L., "Coherent Vortex Structures over a Rotating Spinner Under Non-Axial Inflows at Low Reynolds Number," *54th 3AF International Conference on Applied Aerodynamics*, AERO, Paris, France, 2019, pp. 1–8.

[18] Kobayashi, R., Kohama, Y., Arai, T., and Ukaku, M., "The Boundary-Layer Transition on Rotating Cones in Axial Flow with Free-Stream Turbulence," *JSME International Journal*, Vol. 30, No. 261, 1987, pp. 423–429.

[19] Tambe, S., Schrijer, F., Veldhuis, L., and Gangoli Rao, A., "Spiral Instability Modes on Rotating Cones in High-Reynolds Number Axial Flow Spiral Instability Modes on Rotating Cones in High-Reynolds Number Axial Flow," *Physics of Fluids*, Vol. 34, No. 3, 2022, Paper 034109.
https://doi.org/10.1063/5.0083564

[20] Garrett, S. J., Hussain, Z., and Stephen, S. O., "Boundary-Layer Transition on Broad Cones Rotating in an Imposed Axial Flow," *AIAA Journal*, Vol. 48, No. 6, 2010, pp. 1184–1194.
https://doi.org/10.2514/1.J050021

[21] Drazin, P. G., *Introduction to Hydrodynamic Stability*, Cambridge Univ. Press, Cambridge, England, U.K., 2002, Chap. 2, https://www.cambridge.org/core/product/identifier/9780511809064/type/book.
https://doi.org/10.1017/CBO9780511809064

[22] Hussain, Z., "Stability and Transition of Three-Dimensional Rotating Boundary Layers," Ph.D. Thesis, Univ. of Birmingham, Birmingham, U.K., 2010, http://etheses.bham.ac.uk/839/.

[23] Kato, K., Segalini, A., Alfredsson, P. H., and Lingwood, R. J., "Instabilities and Transition on a Rotating Cone–Old Problems and New Challenges," *IUTAM Laminar-Turbulent Transition, IUTAM Bookseries*, edited by S. Sherwin, P. Schmid, and X. Wu, Vol. 38, Springer, Cham, 2022.
https://doi.org/10.1007/978-3-030-67902-6_17

[24] Kohama, Y., "Study on Boundary Layer Transition of a Rotating Disk," *Acta Mechanica*, Vol. 199, Nos. 3–4, 1984, pp. 193–199, http://link.springer.com/article/10.1007/BF01170959.
https://doi.org/10.1007/BF01170959

[25] Lingwood, R. J., "An Experimental Study of Absolute Instability of the Rotating-Disk Boundary-Layer Flow," *Journal of Fluid Mechanics*, Vol. 314, May 1996, pp. 373–405.
https://doi.org/10.1017/S0022112096000365

[26] Hussain, Z., Garrett, S. J., Stephen, S. O., and Griffiths, P. T., "The Centrifugal Instability of the Boundary-Layer Flow over a Slender Rotating Cone in an Enforced Axial Free Stream," *Journal of Fluid Mechanics*, Vol. 788, Feb. 2016, pp. 70–94.
https://doi.org/10.1017/jfm.2015.671

[27] Gajjar, J. S., "Nonlinear Critical Layers in the Boundary Layer on a Rotating Disk," *Journal of Engineering Mathematics*, Vol. 57, No. 3, 2007, pp. 205–217.
https://doi.org/10.1007/s10665-006-9096-4

S. Fu
Associate Editor